Post-merger Jets from Supermassive Black Hole Coalescences as Electromagnetic Counterparts of Gravitational Wave Emission

Chengchao Yuan[1,2,3] , Kohta Murase[1,2,3,4] , B. Theodore Zhang[1,2,3] , Shigeo S. Kimura[5] , and Péter Mészáros[1,2,3]

[1] Department of Physics, The Pennsylvania State University, University Park, PA 16802, USA; cxy52@psu.edu
[2] Department of Astronomy & Astrophysics, The Pennsylvania State University, University Park, PA 16802, USA; murase@psu.edu
[3] Center for Multimessenger Astrophysics, Institute for Gravitation and the Cosmos, The Pennsylvania State University, University Park, PA 16802, USA
[4] Center for Gravitational Physics, Yukawa Institute for Theoretical Physics, Kyoto University, Kyoto, Kyoto 606-8502, Japan
[5] Frontier Research Institute for Interdisciplinary Sciences; Astronomical Institute, Tohoku University, Sendai 980-8578, Japan

Abstract

As a powerful source of gravitational waves (GW), a supermassive black hole (SMBH) merger may be accompanied by a relativistic jet that leads to detectable electromagnetic (EM) emission. We model the propagation of post-merger jets inside a pre-merger wind bubble formed by disk winds, and calculate multiwavelength EM spectra from the forward shock region. We show that the nonthermal EM signals from SMBH mergers are detectable up to the detection horizon of future GW facilities such as the Laser Interferometer Space Antenna (LISA). Calculations based on our model predict slowly fading transients with time delays from days to months after the coalescence, leading to implications for EM follow-up observations after the GW detection.

Unified Astronomy Thesaurus concepts: Non-thermal radiation sources (1119); Supermassive black holes (1663); Relativistic jets (1390); Gravitational wave sources (677)

1. Introduction

Supermassive black hole (SMBH) mergers are ubiquitous in the history of the universe (Begelman et al. 1980; Kormendy & Ho 2013; Kroupa et al. 2020) and can produce powerful gravitational wave (GW) bursts when they coalesce (e.g., Thorne & Braginskii 1976; Sesana et al. 2004), making them promising candidates for GW detectors such as the Laser Interferometer Space Antenna (LISA, Amaro-Seoane et al. 2017; Baker et al. 2019) and pulsar timing arrays (PTAs, e.g., Mingarelli et al. 2017; Taylor et al. 2019; Arzoumanian et al. 2020) in single-source and/or stochastic GW background searches. The accretion activity between the binary system and the surrounding disk can produce multiwavelength electromagnetic (EM) emission (e.g., Milosavljević & Phinney 2005; Moesta et al. 2012; Farris et al. 2015; Kelly et al. 2017; Haiman 2017; dAscoli et al. 2018), and the time-variable EM signatures from the circumbinary disks could be detectable (e.g., Schnittman & Krolik 2008; Haiman et al. 2009; Tanaka & Menou 2010). The spinning SMBH expected to form after the SMBHs have coalesced may also lead to relativistic jets, in which particle acceleration will take place. The resulting nonthermal emission from the accelerated electrons may provide a promising post-merger EM counterpart of the GW emission, and will not only provide complementary information on SMBH mergers but also shed light on the physical processes in these systems (e.g., Schnittman 2011; Ravi & Array 2018; Mészáros et al. 2019). Yuan et al. 2020 recently suggested that the SMBH mergers can also be high-energy neutrino emitters, and demonstrated that they are also promising targets for high-energy multi-messenger astrophysics (Murase & Bartos 2019).

We study the EM emission produced in relativistic jets launched after the coalescence of SMBHs. The physical picture is that the disk winds originating from the circumbinary disk and mini-disks around each SMBH form a pre-merger wind bubble, and jets powered by the Blandford–Znajek (BZ; Blandford & Znajek 1977) mechanism are launched after the

merger. The jets push ahead inside the pre-merger disk wind material, resulting in the formation of forward and reverse shocks. In the forward shock region, electrons are accelerated to high energies with a power-law distribution as observed in afterglows of gamma-ray bursts (GRBs; e.g., Mészáros 2006). These particles then produce broadband nonthermal EM emission through synchrotron and synchrotron self-Compton (SSC) processes. This Letter is organized as follows. In Section 2, we introduce the physical conditions of the pre-merger wind bubble and model the propagation of jets. The radiation processes and the resulting photon spectra, light curves, and detection horizons are presented in Section 3. In Section 4, we discuss implications of our results. Throughout the Letter, we use the conventional notation $Q_x = Q/10^x$ and physical quantities are written in centimeter-gram-second units, unless otherwise specified.

2. Jet Dynamics

We discuss here the physical conditions in a pre-merger circumbinary environment and derive relevant quantities that describe the jet propagation. We consider on-axis observers, which is sufficient for the purpose of this work. The emission region is typically expected to be only mildly relativistic on timescales of interest (the corresponding observation time after the jet launch is $T \sim 10^5$–10^6 s).

Numerical simulations have demonstrated that binary SMBH mergers can produce jet-like emissions driven by the Poynting outflow (e.g., Kelly et al. 2017). We assume that a jet is launched after the coalescence and subsequently propagates in the wind bubble formed by pre-merger disk winds. Figure 1 schematically illustrates the configuration of the system. The gaseous environment in the host galaxy center, in which the wind bubble expands. We focus on shock interactions between the jet and wind bubble. Initially, the circumbinary disk can react promptly to the evolution of the binary system. The ratio between the disk radius R_d and the semimajor axis of the binary system a remains unchanged ($R_d/a \sim 2$), until the inspiral timescale t_{GW} of the binary system
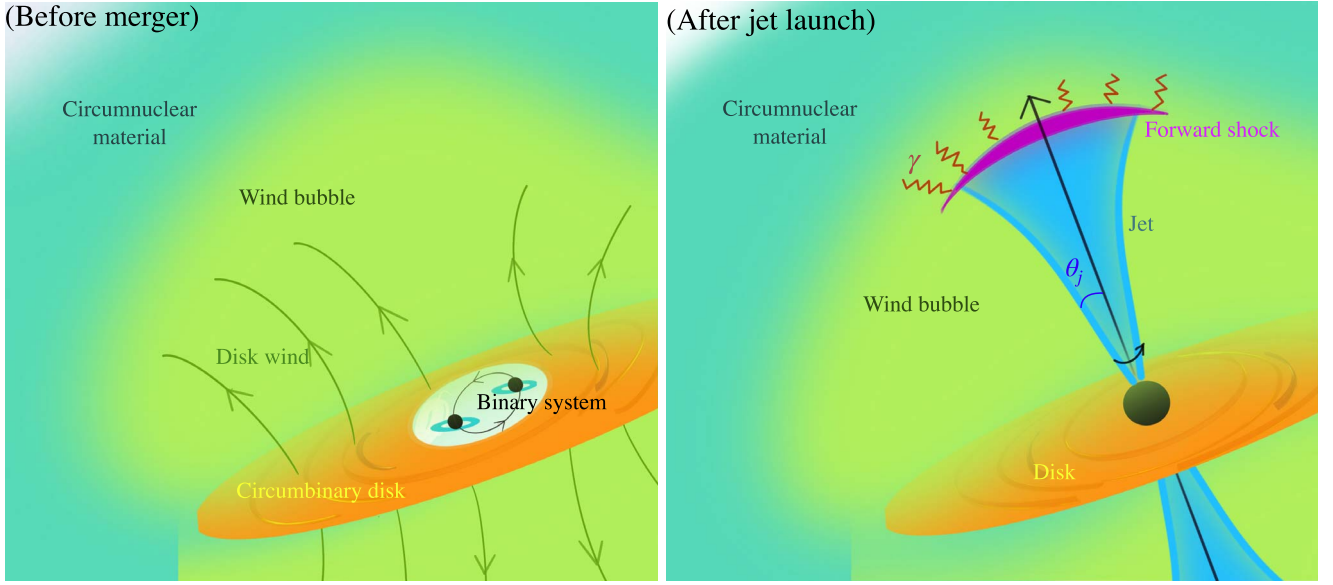
Figure 1. Schematic description of our model. Left panel: pre-merger disk winds launched from the circumbinary disk. The green arrows illustrate the disk-driven outflows that form a wind bubble. Mini-disks around each SMBH are also shown. Right panel: post-merger jets launched by a merged SMBH. The forward shock region is shown as the purple area. The cocoon is not depicted.

(e.g., Shapiro & Teukolsky 1983) equals the viscosity timescale $t_{\rm vis}$ (e.g., Pringle 1981), which is known as the disk decoupling. After the disk becomes decoupled, the merger of SMBHs in binary system occurs within the time interval $t_m \sim 3 \times 10^{-2}$ yr $M_{\rm BH,6}\alpha_{-1}^{-8/5}h_{-1}^{-16/5}$, where $M_{\rm BH} = 10^6 M_{\rm BH,6}M_\odot$ is the mass of the binary system, the dimensionless parameter h is defined as $h = H/R_d$, $\alpha \sim 0.1$ is the viscosity parameter, and H is the disk scale height. The disk gas starts to fill the cavity between the disk and the SMBHs in the viscosity timescale,

$$t_{\rm vis} \sim 0.1 \ {\rm yr} \ M_{\rm BH,6}\alpha_{-1}^{-8/5}h_{-1}^{-16/5} \qquad (1)$$

after the coalescence (Farris et al. 2015). This leads to a time delay ($t_{\rm delay} \sim t_{\rm vis}$) of days to months between the GW burst and the launch of post-merger jets, if $h \sim 0.1$–0.3 is assumed. However, for a thick and highly magnetized disk with $h \sim \alpha \sim 1$, $t_{\rm delay}$ could be much shorter.

On the other hand, within the duration of these two short-term processes, e.g., $t_{\rm m}$ and $t_{\rm vis}$, the disk wind radius may reach $v_d(t_{\rm vis} - t_m) \sim 10^{14} - 10^{16}$ cm above the disk, where v_d is the disk wind velocity that is of the order of the escape velocity, $v_{\rm esc}(R_{d,\rm dec}) \approx \sqrt{2GM_{\rm BH}/R_{d,\rm dec}}$ for the circumbinary disk, and $R_{d,\rm dec} \approx 1.2 \times 10^{13}$ cm $M_{\rm BH,6}\alpha_{-1}^{-2/5}h_{-1}^{-4/5}$ is the radius of the circumbinary disk at the decoupling. In reality, not only the circumbinary disk but also mini-disks around two SMBHs contribute, which would make the wind bubble more complicated. For simplicity, we assume the density profile of the winds at the decoupling to obtain the density distribution of the wind bubble at larger distances,

$$\varrho_w(r) = \frac{\eta_w(1 + \chi)\dot{M}_{\rm BH}}{4\pi r^2 v_d} \equiv Dr^{-2}, \qquad (2)$$

where $\dot{M}_{\rm BH}$ is the mass accretion rate onto the binary system, $\chi \sim 1$ is introduced to take into account the contribution of mini-disks, and η_w represents the fraction of accreted mass converted to the disk wind. According to the simulations, for SANE (Standard And Normal Evolution) models, the parameter η_w may vary from 10^{-4} to 10^{-1} (Jiang et al. 2019b, 2019a; Ohsuga et al. 2009) when

the mass accretion rate changes from sub-Eddington to super-Eddington. In MAD (Magnetically Arrested Disk) models, η_w can reach 10^{-2} to 10^{-1} (Akiyama et al. 2019). With $v_d \sim v_{\rm esc}(R_{d,\rm dec})$, we have $D \simeq 5.9 \times 10^{11}$ g cm^{-1} $\tilde{\eta}_{w,-1.5}(\dot{m}/0.5)M_{\rm BH,6}\beta_{d,-1}^{-1}$, where $\tilde{\eta}_w \equiv (1 + \chi)\eta_w$, $\beta_{d,-1} \equiv v_d/(0.1c)$, the parameter $\dot{m}$ is defined as the ratio of $\dot{M}_{\rm BH}$, and the Eddington value $\dot{M}_{\rm Edd} \equiv 10L_{\rm Edd}/c^2$ (assuming a radiation efficiency of 0.1).

After the coalescence, a powerful jet driven by the spin energy of the newly formed SMBH can appear, subsequently propagating in the pre-merger wind bubble. Considering a sub-Eddington accretion rate with the MAD configuration, we estimate the jet kinetic luminosity to be

$$\begin{aligned} L_{k,j} &= \eta_j \dot{M}_{\rm BH}c^2 \\ &\simeq 6.3 \times 10^{44} \ {\rm erg} \ {\rm s}^{-1}\eta_j(\dot{m}/0.5)M_{\rm BH,6}, \end{aligned} \qquad (3)$$

where $\eta_j \sim 0.3$–1 is the ratio of the accretion energy converted to the jet energy (Tchekhovskoy et al. 2011). Following the standard jet propagation theory (e.g., Bromberg et al. 2011; Mizuta & Ioka 2013), we write down the dimensionless parameter that represents the ratio of the energy density of the jet and the rest-mass energy density of the surrounding medium

$$\tilde{L} \approx \frac{L_{k,\rm iso}}{4\pi r^2 \varrho_w c^3} \simeq 63 \ \tilde{\eta}_{w,-1.5}^{-1}\eta_j\theta_{j,-0.5}^{-2}\beta_{d,-1}, \qquad (4)$$

where θ_j is the jet opening angle, $L_{k,\rm iso} \approx 2L_{k,j}/\theta_j^2$ is the isotropic-equivalent luminosity. Since the quantity $\tilde{L}$ lies in the regime $\theta_j^{-4/3} \ll \tilde{L}$, we expect that the jet is "uncollimated" for our fiducial parameters.[6] This situation is similar to that in choked jet propagation in the circumstellar material (Senno

---

[6] However, jet collimation, which was assumed in Yuan et al. (2020), would be achievable for the super-Eddington accretion accompanied by disk winds with $\eta_w \sim 0.1$–0.3.

et al. 2016; Nakar 2015), and β_h is evaluated from $\tilde{L}$. In the relativistic limit, the jet head Lorentz factor is $\Gamma_h \approx \tilde{L}^{1/4}/\sqrt{2}$ (Senno et al. 2016), and we have $\Gamma_h \sim 2$ in our fiducial case with $\tilde{\eta}_w = 10^{-1.5}$. Note that the jet head radius is $R_h = c\beta_h \hat{T} \approx c\hat{T}$, and $\hat{T}$ is introduced to represent time measured in the central engine frame, which can be converted to the observation time T via $T = (1 + z)(1 - \beta_h)\hat{T}$ (that is $T \approx (1 + z)\hat{T}/[2\Gamma_h^2]$ in the relativistic limit) for on-axis observers.

Furthermore, to ensure particle acceleration, we impose radiation constraints requiring that the shock is collisionless, without being mediated by radiation (Murase & Ioka 2013; Senno et al. 2016). Here, ignoring effects of pair production, we use the conservative condition, $\tau_T \approx \varrho_w \sigma_T R_h / m_p < 1$, where σ_T is the Thomson cross section. Numerically, this condition is satisfied at $\hat{T} \gtrsim 10$ s, which is much shorter than the duration of EM emission.

3. Electromagnetic Emission from the Post-merger Jet

With the jet dynamics presented in the previous section, we calculate the EM spectra resulting from synchrotron and SSC emission. As in the standard theory of GRB afterglows (e.g., Mészáros 2006), we assume that electrons are accelerated at the external forward shock with a power-law spectral index s. The energy fractions of the downstream energy density converted to nonthermal electron and magnetic field energy are defined as ϵ_e and ϵ_B, respectively. The upstream number density is given by $n_{h,u} \approx \varrho_w(R_h)/m_p \propto R_h^{-2}$, and $B \approx [\epsilon_B 32\pi\Gamma_h(\Gamma_h - 1)n_{h,u}m_p c^2]^{1/2}$ is the downstream magnetic field strength.

In the relativistic limit ($\Gamma_h \gg 1$), the characteristic injection frequency ν_m and the cooling frequency ν_c in the observer frame are written, respectively, as,

$$
\begin{aligned}
\nu_m &\approx \frac{3\Gamma_h \gamma_m^2 eB}{4\pi(1 + z)m_e c} \\
&\simeq 3.4 \times 10^3 \text{ GHz } \epsilon_{e,-1}^2 \zeta_{e,-0.4}^2 \epsilon_{B,-2}^{1/2} \eta_j^{1/2} T_4^{-1} \\
&\quad \times (\dot{m}/0.5)^{1/2} M_{\text{BH},6}^{1/2} \theta_{j,-0.5}^{-1}
\end{aligned} \tag{5}
$$

and

$$
\begin{aligned}
\nu_c &\approx \frac{3\Gamma_h \gamma_c^2 eB}{4\pi(1 + z)m_e c} \\
&\simeq 4.6 \times 10^2 \text{ GHz } (1 + z)^{-2}(1 + Y)^{-2}\epsilon_{B,-2}^{-3/2} \\
&\quad \times \tilde{\eta}_{w,-1.5}^{-2} \theta_{j,-0.5}^{-1}(\dot{m}/0.5)^{-3/2} T_4 \beta_{d,-1}^2 M_{\text{BH},6}^{-3/2},
\end{aligned} \tag{6}
$$

where $\gamma_m = \epsilon_e \zeta_e(\Gamma_h - 1)m_p/m_e$ is the electron minimum Lorentz factor, and $\gamma_c = 6\pi m_e c/[(1 + Y)T'\sigma_T B^2]$ is the cooling Lorentz factor. Here, $\zeta_e = g_s/f_e = 1/[f_e \ln(\gamma_M/\gamma_m)] \sim 0.3$–0.4 is constrained by the particle-in-cell simulations (Park et al. 2015) (where f_e is the fraction of accelerated electrons and the maximum Lorentz factor of electrons is $\gamma_M = (6\pi e)^{1/2}/[\sigma_T B(1 + Y)]^{1/2}$), Y is the Compton parameter, and $T' = \hat{T}/\Gamma_h \approx 2\Gamma_h T/(1 + z)$ is the comoving time. For example, at $T = 10^4$ s, we have $Y \simeq 2.4$,

corresponding to the fast cooling regime. It changes to the slow cooling regime on a timescale from days to weeks. We obtain the peak synchrotron flux (e.g., Wijers & Galama 1999)

$$
\begin{aligned}
F_{\nu,\text{syn}}^{\max} &\approx \frac{(1 + z)(0.6f_e n_{h,u}R_h^3)\Gamma_h e^3 B}{\sqrt{3} m_e c^2 d_L^2} \\
&\simeq 0.24 \text{ m Jy } (1 + z)g_{s,-1.2}\zeta_{e,-0.4}^{-1}(\dot{m}/0.5)^{3/2} \\
&\quad \times \eta_j^{1/2}\epsilon_{B,-2}^{1/2}\tilde{\eta}_{w,-1.5}\beta_{d,-1}^{-1}\theta_{j,-0.5}^{-1}M_{\text{BH},6}^{3/2}d_{L,28}^{-2}.
\end{aligned} \tag{7}
$$

The low-frequency synchrotron emission is subject to synchrotron self-absorption (SSA). The SSA optical depth is written as $\tau_{\text{ssa}}(\nu) = \xi_s e n_{h,u}R_h(\nu/\nu_n)^{-p}/[B\gamma_n^5]$, where ν is the observed frequency, $\xi_s \sim 5$–10 depends on the electron spectral index, $\gamma_n = \min[\gamma_m, \gamma_c]$, $\nu_n = \gamma_n^2 eB/[(1 + z)m_e c]$, $p = 5/3$ for $\nu < \nu_n$ and $p = (4 + s)/2$ or $p = 3$ for $\nu > \nu_n$ depending on the slow or fast cooling regime (e.g., Panaitescu & Kumar 2000; Murase et al. 2014). The critical timescales set by $\tau_{\text{ssa}} = 1$ for $\nu < \nu_n$ and for $\nu > \nu_n$ are $T_{\text{ssa}} \simeq 5.4 \times 10^5$ s $\xi_{s,1}^{3/10}(1 + z)^{1/2}$ $(1 + Y)^{1/2}\epsilon_{B,-2}^{3/5}\left(\frac{\nu}{1 \text{ GHz}}\right)^{-1/2}\tilde{\eta}_{w,-1.5}^{11/10}\beta_{d,-1}^{-11/10}(\dot{m}/0.5)^{9/10}M_{\text{BH},6}^{9/10}$ and $T_{\text{ssa}} \simeq 3.5 \times 10^5$ s $\xi_{s,1}^{1/2}(1 + z)^{-1/2}(1 + Y)^{-1/2}M_{\text{BH},6}^{1/2}\left(\frac{\nu}{100 \text{ GHz}}\right)^{-3/2}$ $(\dot{m}/0.5)^{1/2}M_{\text{BH},6}^{1/2}\tilde{\eta}_{w,-1.5}^{1/2}\beta_{d,-1}^{-1/2}$, respectively. Thus, we expect that EM emission at 5 GHz and 100 GHz reaches a peak about a few days after the jet launch ($T_{\text{ssa}} \simeq 7.1 \times 10^5$ s and $T_{\text{ssa}} \simeq 3.1 \times 10^5$ s, respectively, in our fiducial case with $\xi_s = 8.7$).

We numerically calculate the electron distribution and the resulting synchrotron and SSC spectra of the forward shock, following the method used in Murase et al. (2011) and Zhang et al. (2020). We solve the continuity equation that describes the evolution of the electron spectra and calculate the synchrotron/SSC components, in which the trans-relativistic regime can be consistently treated as in Zhang et al. (2020). Combining the obtained radio, millimeter, optical and X-ray light curves with the sensitivities of corresponding detectors, we discuss the possibility of follow-up observations of the EM counterpart.

The left panel of Figure 2 shows the snapshots of synchrotron and SSC spectra at $T = 10^4 - 10^6$ s for an on-axis source located at $z = 1$. We assume $s = 2.0$, $\epsilon_e = 0.1$, and $\epsilon_B = 0.01$. The solid and dashed lines correspond to the synchrotron and SSC components. Very high-energy gamma-ray emission at $\gtrsim 1$ TeV energies is suppressed due to the Klein-Nishina effect (e.g., Murase et al. 2011; Zhang et al. 2020), and the $\gamma\gamma$ annihilation with the extragalactic background light (EBL). For the EBL correction, $\gamma\gamma$ optical depth data from Model C in Finke et al. (2010) is used. To show how the EM signal evolves with time, we illustrate the gamma-ray (1 GeV), X-ray (1 keV), UV (1 eV), and radio (5 GHz and 100 GHz) light curves in the right panel. In particular, before the characteristic time T_{ssa} (shown as the vertical yellow and blue lines). The radio emission is suppressed by the SSA process, which is implemented by multiplying $(1 - e^{-\tau_{\text{ssa}}})/\tau_{\text{ssa}}$.

It is useful to discuss the detection horizon $d_{\lim}$ for some detectors such as the Square Kilometre Array (SKA), Very Large Array (VLA), Expanded VLA (EVLA), Atacama Large Millimeter Array (ALMA), Hubble Space Telescope (HST), James Webb Space Telescope (JWST), Large Synoptic Survey
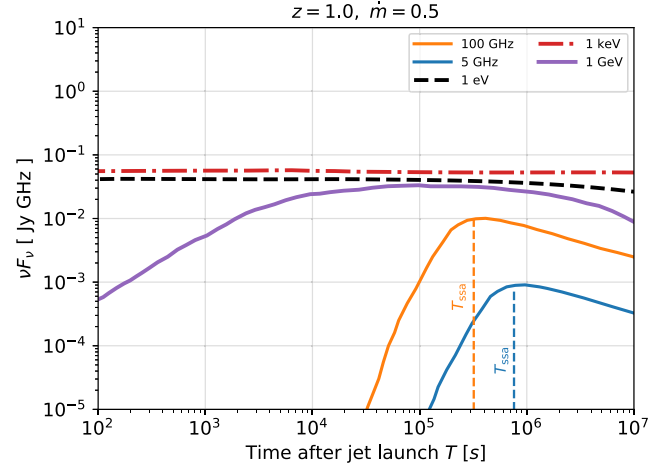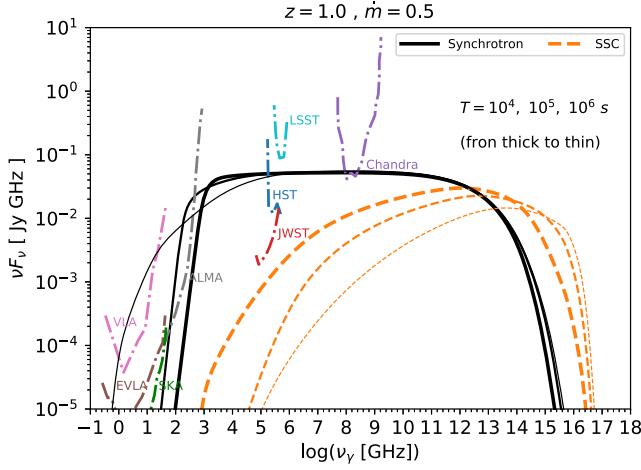
Figure 2. Left panel: nonthermal energy spectra expected for uncollimated post-merger jets from an SMBH merger located at $z = 1$. The solid and dashed lines represent the synchrotron and SSC components. The dashed–dotted lines show the sensitivity curves for current and future detectors. Right panel: multiwavelength light curves. The yellow and blue dashed vertical lines illustrate, respectively, the characteristic times, e.g., T_{ssa}, of 100 GHz and 5 GHz emissions. The used parameters are $\dot{m} = 0.5$, $M_{BH} = 10^6 \, M_\odot$, $\tilde{\eta}_w = 10^{-1.5}$, $\eta_j = 1$, $\theta_j = 10^{-0.5}$, $s = 2.0$, $\zeta_e = 0.4$, $\epsilon_e = 0.1$, and $\epsilon_B = 0.01$.

Telescope (LSST), and the high-resolution camera on the Chandra X-ray Observatory (Chandra)[7] as functions of the observation time T. Given the observed flux $F_\nu(\nu_\gamma, T, z)$ at the observer time T from an on-axis source located at redshift z, the horizon can be calculated iteratively via

$$d_{lim}(\nu_\gamma, T) = d_L \left(\frac{\frac{1}{\Delta T_{exp}} \int_T^{T+\Delta T_{exp}} F_\nu(\nu_\gamma, t, z) dt}{F_{lim}(\nu_\gamma, \Delta T_{exp})} \right)^{1/2}, \quad (8)$$

where $F_{lim}(\nu_\gamma, \Delta T_{exp})$ is the detector sensitivity normalized to the exposure time ΔT_{exp}. For example, specifying the detection frequency $\nu = 100$ GHz, the sensitivity of ALMA is approximately $34 \, \mu$Jy for a 1 hr integration, e.g., $\Delta T_{exp} = 1$ hr. Figure 3 indicates the detection horizons for SKA (5 GHz, $\Delta T_{exp} = 10$ hr), SKA (1 GHz[8], $\Delta T_{exp} = 10$ hr), VLA (5 GHz, $\Delta T_{exp} = 1$ hr), ALMA (100 GHz, $\Delta T_{exp} = 1$ hr), JWST (1 eV, $\Delta T_{exp} = 10$ ks), HST (1 eV, $\Delta T_{exp} = 10$ ks), LSST (r-band, point source exposure time $\Delta T_{exp} = 30$ s in the 3 day revisit time), and Chandra (1 keV, $\Delta T_{exp} = 100$ ks). The vertical black and blue dotted lines, respectively, illustrate the times T_{ssa} at which photons at 100 GHz and 5 GHz bands start to survive from the synchrotron self-absorption.

From Figure 3, we expect that ALMA, SKA, and EVLA can detect SMBH mergers in the radio bands, respectively, out to redshifts of $z \sim 4$–6. Remarkably, the optical and X-ray signals from the mergers in the range of $1 \lesssim z \lesssim 2$ can also be identified through targeted searches by Chandra, HST, and JWST in a long duration after the merger. In addition, we can estimate the observation time for each detector if the luminosity distance of the merger is specified. For example, a source located at $z = 3$ would remain detectable by ALMA for roughly 20–30 days (see the black dotted horizontal line). One caveat is
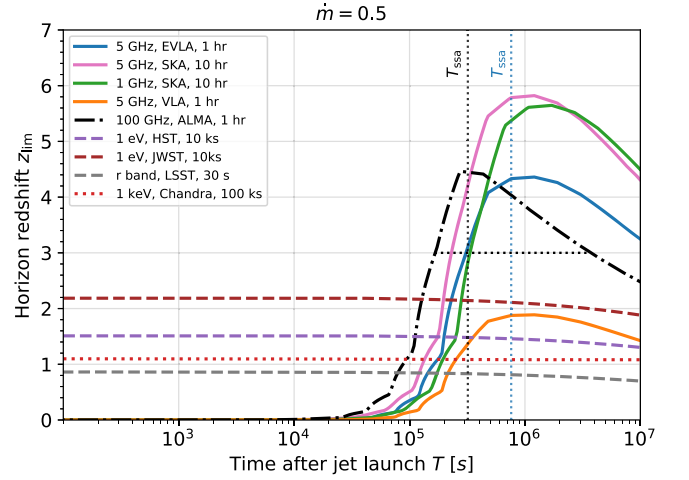
Figure 3. Detection horizons for multiwavelength detectors, e.g., SKA, VLA, EVLA, ALMA, HST, JWST, LSST, and Chandra. The horizontal dotted line shows the 100 GHz detection window for ALMA assuming a source located at $z = 3$. Similar to Figure 2, the dotted vertical lines are the characteristic times of 5 GHz and 100 GHz signals.

that this calculation is carried out in the ideal case where the detectors can point to the position of the source and start the observation immediately after the EM signal reaches the Earth. We discuss the sky coverage and a detection strategy in the following Section 4.

4. Summary and Discussion

We investigated broadband nonthermal EM emission from electrons accelerated at the external forward shock expected in post-merger jets from the coalescence of SMBHs. In our model, the jets can be launched at $t_{delay} \sim t_{vis} \sim (0.003$–$0.1)M_{BH,6}$ yr after the coalescence. The time lag is primarily determined by the scale height of the circumbinary disk and the viscosity parameter. We found that, for a moderate accretion rate ($\dot{m} \sim 0.5$), the multiwavelength emission from such a system may persist at detectable levels for months after the jet launch, depending on the facilities and the luminosity distance. Moreover, according to our model, the sources with moderate $\dot{m} = 0.5$ can be detected up to $z \sim 5$–6, covering the

range that LISA-like GW detectors have the best detection chance, e.g., $z \sim 1$–2, in which $(1$–$10)f_b$ mergers per year are expected (Menou et al. 2001; Enoki et al. 2004; Arun et al. 2009; Amaro-Seoane et al. 2012; Dal Canton et al. 2019; Kara et al. 2019). Here $f_b \sim 1/(2\Gamma_h^2)$ is the beaming factor in our model. Because the jet head Lorentz factor is as low as $\Gamma_h \lesssim 2$, the EM emission from the forward shock region is not highly beamed and we expect $f_b \sim 0.1$–1. This makes the binary SMBH mergers interesting targets for future multi-messenger studies. If super-Eddington accretion (e.g., $\dot{m} \sim 10$) occurs, as was optimistically assumed in Yuan et al. (2020), even LSST and Chandra could detect EM signals from the sources in the redshift range $4 \lesssim z \lesssim 6$. We showed the case of $s = 2.0$ for the demonstration. If a larger spectral index, e.g., $s \sim 2.2$–2.4, is used, as expected from observations of GRB afterglows, the radio detection would be more promising whereas a higher accretion rate would be required for successful optical and X-ray observations.

The density of the pre-merger bubble, which was assumed to be a wind profile, is subject to large uncertainties. The extrapolation in the density distribution would be applicable up to an outer wind radius of $\sim 10^{14}$–10^{16} cm. The density predicted by Equation (2) would drop below that of the central molecular zone (indicated as the circumnuclear environment in Figure 1), which may lead to an increased radio emission. In addition, a cocoon formed along with the jet, depending on uncertain details of the medium, could produce thermal photons, which may not only lead to detectable signals but also serve as seed photons for inverse-Compton emission. We focused on the more secure EM emission from the forward shock region as the jet propagates in the wind. In this sense, our prediction for the fluxes are conservative.

EM emission from the external reverse shock and internal shocks can also be expected (e.g., Mészáros & Rees 1999; Kobayashi & Zhang 2003, for the reverse shock emission in GRBs). Qualitatively, the ratio between the peak fluxes of the reverse and forward shock emission depends on the value of Γ_j, and the reverse shock contribution might be important for $\Gamma_j \gg \Gamma_h$.

Previous studies based on general relativistic three-dimensional magnetohydrodynamics simulations have shown that the circumbinary disk and the corona can emit light in UV/EUV bands (e.g., dAscoli et al. 2018), while X-ray and infrared emission from the post-merger circumbinary disk are expected to last for years (Milosavljević & Phinney 2005; Schnittman & Krolik 2008). In the pre-merger phase, the orbits of dual SMBH cores may be identified by radio facilities such as VLBI (e.g., Rodriguez et al. 2006). Blind searches could identify radio or UV/EUV sources from the binary SMBH systems, which would provide complementary constraints on the source location, the accretion rate, and the ambient gaseous environment.

Our model can provide a guidance, including the onset times and the detection windows, in developing detection strategies for future EM follow-up observations, once GW signals are detected. Considering the large uncertainties in the localization with GW detectors, an initial follow-up using large field-of-view (FOV) telescopes, like SKA and LSST, would be necessary to more precisely localize the position of the source. After that, we can use the putative positional information from the initial follow-up imaging to guide the observation of narrower FOV telescopes. In particular, for high-redshift

mergers in the range $z \sim 2$–5, EM follow-up observations rely more on radio detectors, and the detection is possible a few weeks after the merger. SKA needs the source localization before follow-up observations by VLA and ALMA. On the other hand, if the merger is close enough (e.g., $z \sim 1$), LISA observations starting from a few weeks before the merger can localize the merger with a median precision of $\sim 1 \deg^2$ (Mangiagli et al. 2020). In this case, LISA and LSST can jointly guide other X-ray and optical facilities in the very early stage. Amid these two regimes, e.g., $z \sim 1$–2, detections in the optical and X-ray bands using HST, JWST, and Chandra would be promising once the source is localized by SKA.

ORCID iDs

Chengchao Yuan ⓘ https://orcid.org/0000-0003-0327-6136
Kohta Murase ⓘ https://orcid.org/0000-0002-5358-5642
B. Theodore Zhang ⓘ https://orcid.org/0000-0003-2478-333X
Shigeo S. Kimura ⓘ https://orcid.org/0000-0003-2579-7266

References

Akiyama, K., Alberdi, A., Alef, W., et al. 2019, ApJL, 875, L5
Amaro-Seoane, P., Aoudia, S., Babak, S., et al. 2012, CQGra, 29, 124016
Amaro-Seoane, P., Audley, H., Babak, S., et al. 2017, arXiv:1702.00786
Arun, K., Babak, S., Berti, E., et al. 2009, CQGra, 26, 094027
Arzoumanian, Z., Baker, P. T., Blumer, H., et al. 2020, ApJL, 905, L34
Baker, J., Barke, S. F., Bender, P. L., et al. 2019, 51, 243, arXiv:1907.11305
Begelman, M. C., Blandford, R. D., & Rees, M. J. 1980, Natur, 287, 307
Blandford, R. D., & Znajek, R. L. 1977, MNRAS, 179, 433
Bromberg, O., Nakar, E., Piran, T., et al. 2011, ApJ, 740, 100
Dal Canton, T., Mangiagli, A., Noble, S. C., et al. 2019, ApJ, 886, 146
dAscoli, S., Noble, S. C., Bowen, D. B., et al. 2018, ApJ, 865, 140
Enoki, M., Inoue, K. T., Nagashima, M., & Sugiyama, N. 2004, ApJ, 615, 19
Farris, B. D., Duffell, P., MacFadyen, A. I., & Haiman, Z. 2015, MNRAS, 447, L80
Finke, J. D., Razzaque, S., & Dermer, C. D. 2010, ApJ, 712, 238
Haiman, Z. 2017, PhRvD, 96, 023004
Haiman, Z., Kocsis, B., Menou, K., Lippai, Z., & Frei, Z. 2009, CQGra, 26, 094032
Jiang, Y.-F., Blaes, O., Stone, J. M., & Davis, S. W. 2019a, ApJ, 885, 144
Jiang, Y.-F., Stone, J. M., & Davis, S. W. 2019b, ApJ, 880, 67
Kara, E., Margutti, R., Keivani, A., et al. 2019, BAAS, 51, 112, arXiv:1903.05287
Kelly, B. J., Baker, J. G., Etienne, Z. B., Giacomazzo, B., & Schnittman, J. 2017, PhRvD, 96, 123003
Kobayashi, S., & Zhang, B. 2003, ApJL, 582, L75
Kormendy, J., & Ho, L. C. 2013, ARA&A, 51, 511
Kroupa, P., Subr, L., Jerabkova, T., & Wang, L. 2020, MNRAS, 498, 5652
Mangiagli, A., Klein, A., Bonetti, M., et al. 2020, PhRvD, 102, 084056
Menou, K., Haiman, Z., & Narayanan, V. K. 2001, ApJ, 558, 535
Mészáros, P. 2006, RPPh, 69, 2259
Mészáros, P., Fox, D. B., Hanna, C., & Murase, K. 2019, NatRP, 1, 585
Mészáros, P., & Rees, M. J. 1999, MNRAS, 306, L39
Milosavljević, M., & Phinney, E. S. 2005, ApJL, 622, L93
Mingarelli, C. M. F., Lazio, T. J. W., Sesana, A., et al. 2017, NatAs, 1, 886
Mizuta, A., & Ioka, K. 2013, ApJ, 777, 162
Moesta, P., Alic, D., Rezzolla, L., Zanotti, O., & Palenzuela, C. 2012, ApJL, 749, L32
Murase, K., & Bartos, I. 2019, ARNPS, 69, 477
Murase, K., & Ioka, K. 2013, PhRvL, 111, 121102
Murase, K., Thompson, T. A., & Ofek, E. O. 2014, MNRAS, 440, 2528
Murase, K., Toma, K., Yamazaki, R., & Mészáros, P. 2011, ApJ, 732, 77
Nakar, E. 2015, ApJ, 807, 172

Ohsuga, K., Mineshige, S., Mori, M., & Kato, Y. 2009, PASJ, 61, L7
Panaitescu, A., & Kumar, P. 2000, ApJ, 543, 66
Park, J., Caprioli, D., & Spitkovsky, A. 2015, PhRvL, 114, 085003
Pringle, J. 1981, ARA&A, 19, 137
Ravi, V. 2018, in ASP Conf. Ser., 517, Science with a Next Generation Very
    Large Array, ed. E. Murphy (San Francisco, CA: ASP), 781
Rodriguez, C., Taylor, G. B., Zavala, R. T., et al. 2006, ApJ, 646, 49
Schnittman, J. D. 2011, CQGra, 28, 094021
Schnittman, J. D., & Krolik, J. H. 2008, ApJ, 684, 835
Senno, N., Murase, K., & Mészáros, P. 2016, PhRvD, 93, 083003

Sesana, A., Haardt, F., Madau, P., & Volonteri, M. 2004, ApJ, 611, 623
Shapiro, S. L., & Teukolsky, S. A. 1983, Black Holes, White Dwarfs, and
    Neutron Stars: The Physics of Compact Objects (New York: Wiley)
Tanaka, T., & Menou, K. 2010, ApJ, 714, 404
Taylor, S. R., Burke-Spolaor, S., Baker, P. T., et al. 2019, BAAS, 51, 336
Tchekhovskoy, A., Narayan, R., & McKinney, J. C. 2011, MNRAS, 418, L79
Thorne, K. S., & Braginskii, V. 1976, ApJL, 204, L1
Wijers, R., & Galama, T. 1999, ApJ, 523, 177
Yuan, C., Murase, K., Kimura, S. S., & Mészáros, P. 2020, PhRvD, 102, 083013
Zhang, B. T., Murase, K., Veres, P., & Mészáros, P. 2020, arXiv:2012.07796